A new mechanism for filament disconnection at the X-point: poloidal shear in radial $\mathbf{E} \times \mathbf{B}$ velocity

F. Nespoli[1,*], P. Tamain[2], N. Fedorczak[2], D. Galassi[3], Y. Marandet[4]

[1] *Princeton Plasma Physics Laboratory, 100 Stellarator Road, Princeton, NJ 08540, United States of America*
[2] *IRFM, CEA Cadarache, F-13108 St. Paul-lez-Durance, France*
[3] *École Polytechnique Fédérale de Lausanne (EPFL), Swiss Plasma Center (SPC), 1015 Lausanne, Switzerland*
[4] *Aix Marseille Univ, CNRS, PIIM UMR 7345, Marseille, France*
[*] *work performed at affiliation 4. Email: fnespoli@pppl.gov*

Abstract

Plasma filaments generated by turbulence in the scrape-off layer are sometimes observed in experiments and simulations to disconnect from the target plate in the vicinity of the X-point, resulting in a "quiescent zone" with reduced fluctuations, possibly affecting the fluctuating part of the divertor heat loads. This phenomena is usually explained by the flux tubes squeezing, induced by flux expansion, down to scales where collisions dominate. In this work, we consider an additional mechanism spontaneously arising at the X-point: the poloidal shear in radial $\mathbf{E} \times \mathbf{B}$ velocity. Through a simple model, tested against 3D global turbulence simulations, we quantify the effectiveness of this disconnection mechanism and identify ways to control it.

1   Introduction

Plasma filaments, also referred to as blobs, are generated spontaneously at the edge of the toroidally confined plasmas by turbulence through charge separation due to charge-dependent drifts [1]. In the commonly accepted description, they are generated by interchange type instabilities in the zone of bad curvature (typically the low field side close to the outboard midplane) and the perturbation extends along the field lines towards the limiter or divertor plates, to which they are in general electrically connected. Filaments are self-propelled radially outwards by an internal $\mathbf{E} \times \mathbf{B}$ drift. Under certain conditions, they can disconnect from the target plates increasing their radial velocity i.e. the aging of a reactor first wall. Furthermore, they are believed to impact and, under certain circumstances, even completely determine the scrape-off layer (SOL) width [2, 3]. The understanding of filamentary transport is therefore crucial for the physics of the SOL and for the correct prediction of the heat loads on the first wall.

Recently, experimental measurements involving fast framing imaging in the MAST [4] and NSTX [5, 6] tokamaks gave indications that the filaments disconnect from the target plates close to the X-point. This results in MAST in a "quiescent zone" close to the X-point, where the plasma fluctuations are substantially reduced. A similar phenomena has been observed in turbulence simulations of the COMPASS [7] and WEST [8] tokamaks using the flux-driven turbulence code TOKAM3X [9]. In NSTX, the disconnection of the midplane filament from the divertor results, in the proximity of the strike point, in a decrease of the fluctuation level with respect to rest of the SOL [10]. Decorrelation of turbulence across the X-point region has also been observed in simulations with both the BOUT [11] and ArbiTER [12] codes.

The disconnection of filaments at the X-point is usually explained by the flux tubes squeezing, induced by flux expansion, down to scales where collisions dominate [13]. In this work, we consider

an additional mechanism for blob disconnection spontaneously arising at the X-point: the poloidal shear in radial $\mathbf{E} \times \mathbf{B}$ velocity. The rest of the paper is structured as follows: in section 2 we discuss the results of the TOKAM3X simulations showing blob disconnection at the X-point, resulting in the formation of a quiescent zone. In section 3 we discuss the disconnection of filaments at the X-point through flux expansion driven squeezing of the flux tubes. In section 4 we consider an additional mechanism for the disconnection of blobs at the X-point, namely the poloidal shear in radial $\mathbf{E} \times \mathbf{B}$ velocity, spontaneously arising in the presence of an X-point. In section 5 we derive, in steps of increasing complexity, a condition for the effectiveness of this disconnection mechanism. Finally, in section 6, we compare the two considered mechanisms for blob disconnection and we discuss the implications for plasma operation.

2   Quiescent zone in TOKAM3X simulations

Throughout this paper, to support our reasoning, we will use results from TOKAM3X simulations. TOKAM3X [9] is a flux-driven fluid code modeling turbulence in the plasma edge and SOL in realistic magnetic geometry. Throughout this paper we will focus mainly on the simulations described in details in Ref. [8], modeling the edge and SOL of the WEST tokamak in isothermal approximation ($T_e = T_i = T_0$), with T_e and T_i the electron and ion plasma temperature respectively, and T_0 the reference value for plasma temperature. In these simulations, lengths and times are expressed in units of the sound speed ion Larmor radius ρ_s and of ω_c^{-1} respectively, with ω_c the ion cyclotron frequency. In Ref. [8] the blob 3D structure and dynamics have been investigated in detail complementing different analysis techniques such as 2D and 3D conditional average sampling and blob tracking. As a result, it was shown how the filaments connected to the outer midplane (OMP) terminate in correspondence of the X-point when close to the separatrix. One of such filaments, as detected from the 3D blob recognition and tracking algorithm (BRAT) is shown in Fig. 1, color
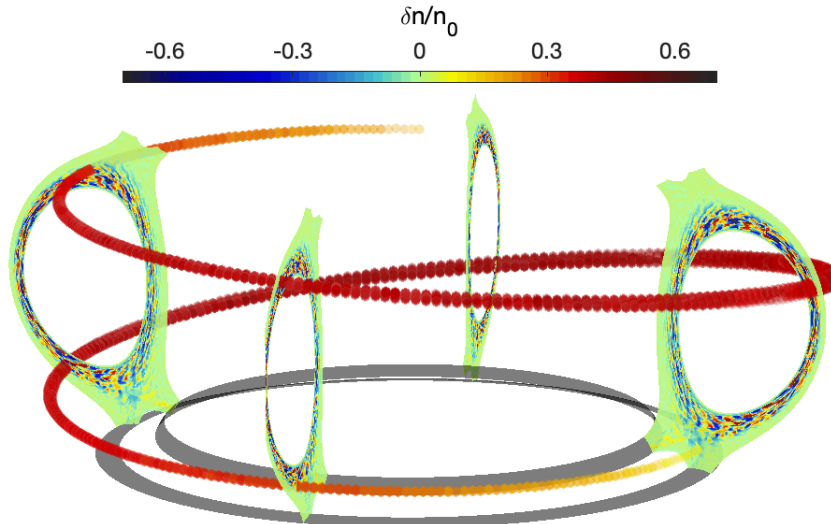

Figure 1: Snapshot of a low-field side filament terminating in the vicinity of the X-point, as detected from the 3D blob recognition and tracking algorithm [8] in TOKAM3X simulation of the WEST tokamak, color coded with the normalized density fluctuation $\delta n / n_0$. The divertor plates are plotted in black. $\delta n / n_0$ is also shown for four different poloidal planes.
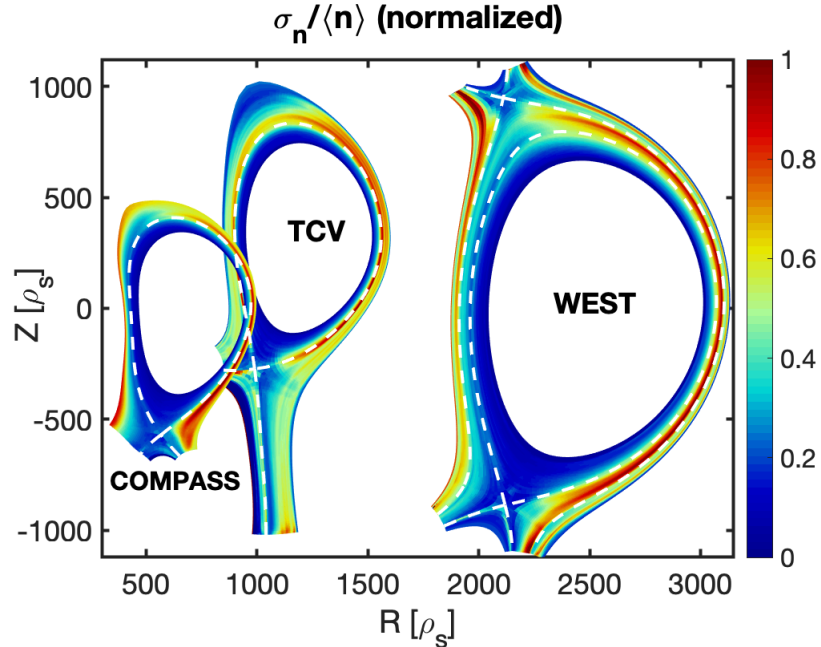
Figure 2: Relative fluctuation level $\sigma_n/\langle n \rangle$ normalized to their maximum value for each simulation, in COMPASS, TCV, and WEST geometry (from left to right).

coded with the density fluctuation $\delta n/n_0$, also plotted on four different poloidal planes, with n_0 the reference value for density. In Fig. 2 we show the relative fluctuation level $\sigma_n/\langle n \rangle$, where σ_n is the standard deviation over time of the plasma density n and the brackets denote average over toroidal direction and time, normalized to the maximum value at the OMP in order to compare the different configurations. As it emerges from the picture, as one approaches the X-point the fluctuation level is reduced by a factor $\gtrsim 3$ with respect to its value in the main SOL, resulting in a "quiescent zone" caused by the disconnection of the filaments. Below the X-point, the fluctuation level remains low along the divertor leg all the way to the divertor plate. Here, the relative fluctuation level $\sigma_n/\langle n \rangle \leq 0.39$ (corresponding to a normalized value of 1.02 in Fig. 2)in the far SOL, and decreases monotonically as one moves radially inwards towards the strike point, where $\sigma_n/\langle n \rangle$=0.07 (normalized value 0.18). A similar decrease of the fluctuation level is observed in correspondence of the secondary X-point at the top of the plasma.

In Fig. 2 the normalized relative fluctuation level is also shown for TOKAM3X isothermal simulations in COMPASS (analyzed in details in Ref. [14]) and TCV geometry, respectively. For the three simulations, with different size, resolution and grid geometry, a similar reduction of the fluctuation level in the vicinity of the X-point is observed, suggesting that this phenomena is not linked to the details of the magnetic configuration and/or the grid used for the simulations and could occur in all diverted plasmas.

3 Flux tube squeezing at the X-point

In the following, we discuss the possible mechanisms responsible for the disconnection of filaments at the X-point. We consider a blob at radial upstream position r_0 of radial and poloidal size at the midplane a_r and a_θ, respectively. The flux expansion in correspondence of the X-point at this
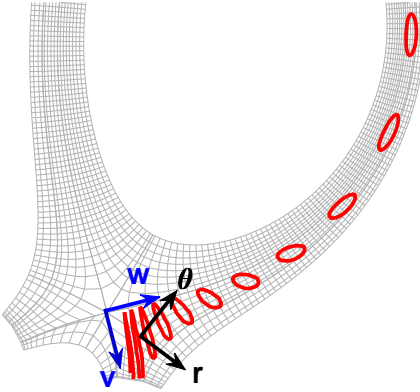
Figure 3: Deformation of the flux tube associated with a blob (in red) as resulting from field line tracing for the magnetic geometry used in the WEST TOKAM3X simualtion (coarser grid shown in grey). The poloidal coordinates (r, θ) and the one used in Ref. [13] (v, w) are shown in black and blue respectively in correspondence of the X-point.

radial position is f_x. In tokamaks, a_θ has been measured to vary from a few to a few hundreds ρ_s [2], with the typical value of $\sim 20\rho_s$ [15, 16, 17, 18, 19], and typically the blob poloidal cross section has elliptical shape with $a_\theta > a_r$. The main cause of blob disconnection at the X-point is so far considered to be the squeezing and tilting of the flux tubes as they go through the high flux expansion and magnetic shear region in correspondence of the magnetic null, down to spatial scales where collisional processes dominate, finally decoupling the perturbations in the upstream SOL from the ones in the divertor leg [13]. An example of the flux tube deformation is shown in Fig. 3. Following Ref. [13], as the flux tube associated with the filament with poloidal size a_θ at the midplane approaches the X-point region, it stretches in the direction parallel to the separatrix leg (v in Fig. 3) accordingly to the flux expansion $f_x \sim B_{p,OMP}/B_p$, where B_p is the poloidal field and $B_{p,OMP}$ its value at the OMP for the same flux surface. In order to conserve its magnetic flux, the filament also squeezes in the direction perpendicular to the separatrix leg (w in Fig. 3) by the same factor f_x. We can consider the flux expansion to effectively damp the density fluctuation associated to the OMP filament when its poloidal size becomes $a_{w,X} \lesssim a_{min}$, where the $_X$ subscript denotes the X-point poloidal location, $a_{min} \sim \rho_s$ is the scale where collisional processes become important, and ρ_s is the sound speed Larmor radius. This disconnection mechanism is therefore effective for

$$f_x \gtrsim a_\theta/a_{min} \tag{1}$$

The latter is always satisfied in the direct vicinity of the X-point as f_x diverges by definition, and more generally on a layer whose thickness depends on the details of the magnetic configuration (radial profile of f_x) and on the size of the blobs at the OMP a_θ. Though, this condition also means that at a given radial position, all filaments with large enough poloidal extension $a_\theta/\rho_s \gtrsim f_x$ can survive the X-point squeezing and extend further towards the target plate.

4 Poloidal shear in radial $\mathbf{E} \times \mathbf{B}$ velocity at the X-point

We consider here an additional mechanism involved in the disconnection of the blobs at the X-point, namely the poloidal shear in radial $\mathbf{E} \times \mathbf{B}$ velocity. As we will show in this section, this shear layer

arises spontaneously in diverted plasmas at the X-point as the topology of the region adjacent to the SOL changes from closed to open field lines, and it is therefore to be found universally in all diverted plasmas, with some exceptions that will be discussed later. Indeed, the commonly accepted description of the divertor leg below the X-point is the one depicted in Ref. [20], and summarized in the following. The plasma enters the divertor at the X-point with an exponentially decaying density in the SOL $n(x) = n_X \exp(-r/\lambda)$, with λ the SOL width and n_X the density at the X-point, and diffuses along the divertor leg and into the private flux region. In the following we use the coordinate system (r, θ, z) such that r is the radial coordinate remapped at the outer midplane, $r = 0$ at the separatrix and increasing in the SOL; θ is the coordinate along the poloidal direction and z is the coordinate along the magnetic field. Both θ and z are null at the X-point location and increase towards the target. The plasma density is described by the continuity equation

$$\partial_t n + \nabla \cdot (n(v_{||} + v_\perp)) = \nabla \cdot (D \nabla_\perp n) \tag{2}$$

which, assuming steady-state condition, uniform parallel velocity $v_{||}$ and diffusion coefficient D and neglecting the drifts velocities $v_\perp$ can be rewritten in our coordinate system as $D\nabla_r^2 n = v_{||}\nabla_z n$. The plasma density $n(r, z)$ is therefore solution of the classic heat diffusion equation with boundary condition $n(r, z = 0) = n_X \exp(-r/\lambda)$ resulting, for $z \geq 0$, in

$$n(r, z) = \frac{n_X}{2} \exp\left[\left(\frac{S}{2\lambda}\right)^2 - \frac{r}{\lambda} \right] \mathrm{erfc}\left(\frac{S}{2\lambda} - \frac{r}{S} \right) \tag{3}$$

with $n_X = n(r = 0, z = 0)$ the density at the X-point and S the spreading factor

$$S = S(z) = \sqrt{\frac{4Dz}{v_{||}}}. \tag{4}$$

We recall that, in this description, S is a function of z and of the transport parameters D and $v_{||}$. This is indeed a good description of the density distribution in the divertor leg in our simulations, as it is shown in Fig. 4a for the WEST case. Here, the parallel profile of plasma density n is plotted at different positions in the SOL along the parallel coordinate z, from the X-point location ($z = 0$) up to the target plate (thick black line in the picture). In the figure, the fit with Eq. (3) is shown with a red line for the parallel profile taken at the radial position the closest to the separatrix, leading to $D = 10^{-3}\rho_s^2\omega_c$ and $\lambda = 1.1\rho_s$, resulting in a good agreement in the near SOL.

Such density distribution along the divertor leg exhibits a strong gradient in the parallel direction. This induces in turn a parallel gradient in the plasma potential as well, as it is shown in Fig. 4b. Indeed, from parallel force balance

$$n\eta j_{||} = \nabla_{||}P_e + 0.71 n\nabla_{||}T_e - n\nabla_{||}\phi \tag{5}$$

and neglecting the first term (typically the resistivity $\eta < 10^{-5}$) and in isothermal approximation ($\nabla_{||}T_e = 0$, $\nabla_{||}P_e = T_e\nabla_{||}n$), we can write

$$\frac{\nabla_{||}n}{n} \sim \frac{\nabla_{||}\phi}{T_e} \tag{6}$$

and the same relation holds for the gradients in the poloidal (θ) direction due to the toroidal symmetry of the system. This results in a radially directed $\mathbf{E} \times \mathbf{B}$ drift

$$v_r = -\frac{\nabla_\theta\phi \times \mathbf{B}}{B^2} = -\frac{T_e}{B}\frac{\nabla_\theta n}{n} \tag{7}$$
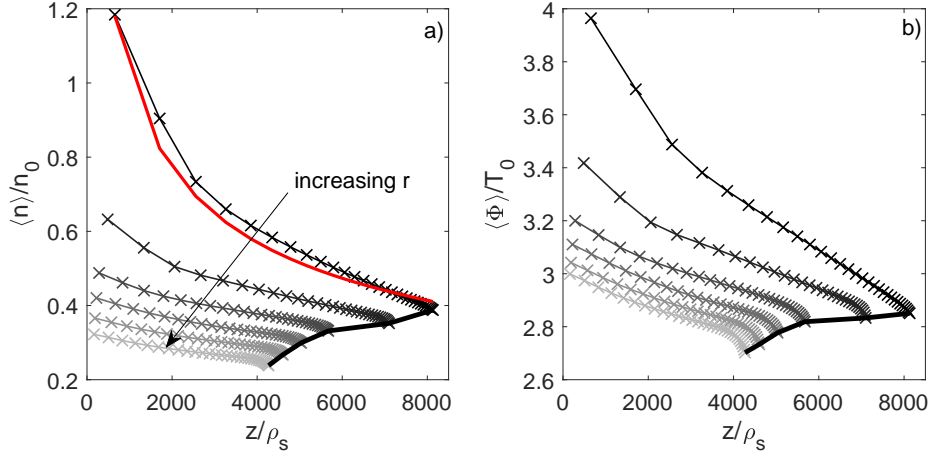
5

Figure 4: Parallel profiles along the outer divertor leg of averaged a) plasma density n b) plasma potential for different values of the radial coordinate r in the SOL. In a), the fit of the profile the closest to the separatrix with Eq. (3) is shown with a red line. The thick black line shows the position of the divertor plate.

where we used the approximation $B_t \sim B$ for the toroidal magnetic field B_t, valid in the vicinity of the X-point.

The radial velocity given by Eq. (7) also decreases (in absolute value) along the divertor leg, resulting finally in a shear layer just below the X-point. Such result is confirmed by our simulations, how it emerges from Fig. 5, where we plot the radial component of the $\mathbf{E} \times \mathbf{B}$ velocity in the surroundings of the X-point for the WEST case. Here, the shear layer extends poloidally over approximately four simulation cells, corresponding to a poloidal span of $l_\theta \sim 53\rho_s$, corresponding to a segment of field
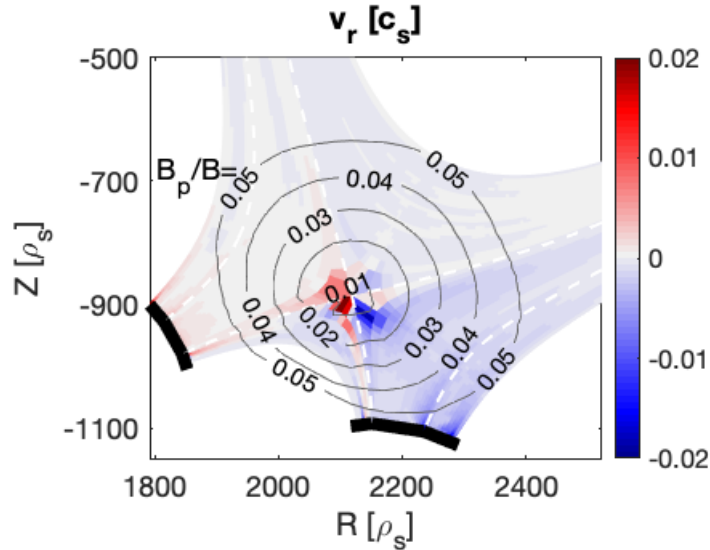

Figure 5: Radial component of the $\mathbf{E} \times \mathbf{B}$ velocity in the surroundings of the X-point, averaged over time and the toroidal direction. The contour levels of B_p/B are also shown with the relative values.

6

line of parallel length 2143 ρ_s, with a variation in radial velocity of approximately $\Delta v_r / c_s \sim 0.02$. We remark that this result is in first approximation independent of the direction of the magnetic field, whose reversal would result in the change of sign for the $\mathbf{E} \times \mathbf{B}$ velocity but not its absolute value and the shearing rate.

Finally, we remark that this model of the divertor leg and therefore of the shear layer below the X-point is valid as long as the plasma density n is decreasing along the divertor leg, i.e. always in divertor sheath limited regime, and also in high-recycling and detached regimes, as long the X-point is sufficiently far from the divertor plates/detachment front so that in the vicinity of the X-point n is still decreasing towards the target. The other cases, where the density gradient along the divertor leg are reversed, could still result in shear layer at the X-point but can not be described by the model exposed here and would need to be addressed in detail in future works.

5   Effectiveness of disconnection through $\mathbf{E} \times \mathbf{B}$ shear

In this section we derive, in steps of increasing complexity, a condition for this disconnection mechanism to be effective. For each of these approximations, we compare with the simulation results. In this process, several assumptions and approximations are used, which are necessary to the final aim of having an analytical expression for the aforementioned condition. Nevertheless, the assumptions made are always conservative, providing an underestimation of the effectiveness of this disconnection mechanism, that has to be regarded as a lower limit. This approach is justified a posteriori by the comparison with the simulation results, showing how the condition derived under these restrictive assumptions is still satisfied, and provides a baseline for future works.

5.1   Local approximation

As a first approximation the poloidal shear of radial velocity can locally compete with parallel dynamics, and therefore help in disconnecting the filaments at the X-point, when

$$\frac{\tau_{||}}{\tau_{sh,\theta}} = \frac{\Delta L_{||}}{c_s} \frac{\Delta v_r}{\Delta L_\theta} = \frac{B}{B_p} \frac{\Delta v_r}{c_s} \gtrsim 1 \tag{8}$$

where we compare the shearing time $\tau_{sh,\theta} = (\Delta v_r / \Delta L_\theta)^{-1}$ with the characteristic time of the parallel dynamics for this problem $\tau_{||} = \Delta L_{||} / c_s$, where we assumed that the perturbation associated with the blob travels along the field line at the sound speed c_s. Δv_r is the variation of the radial velocity across the shear layer of poloidal width ΔL_θ, corresponding to a portion of the field line of length $\Delta L_{||}$. This condition is satisfied in the vicinity of the X-point for our simulations, as it emerges from Fig. 5, where the radial component of the $\mathbf{E} \times \mathbf{B}$ velocity is shown, averaged over time and the toroidal direction, together with the contour levels of B_p / B. Indeed, across the poloidal shear layer $\Delta v_r / c_s \sim 0.02$, which is bigger than B_p / B in the shear layer region.

The condition in Eq. (8) can also be applied locally to each simulation cell, with Δv_r the variation of the radial velocity in the poloidal direction across the simulation cell. The result is shown in Fig. 6, where $\log_{10}\left(\dfrac{B}{B_p} \dfrac{\Delta v_r}{c_s}\right)$ is plotted for the WEST simulation. As it emerges from the figure, $\dfrac{B}{B_p} \dfrac{\Delta v_r}{c_s}$ is of order unity around the X-point, implying that the poloidal shear of radial velocity can compete with the parallel dynamics in this region.
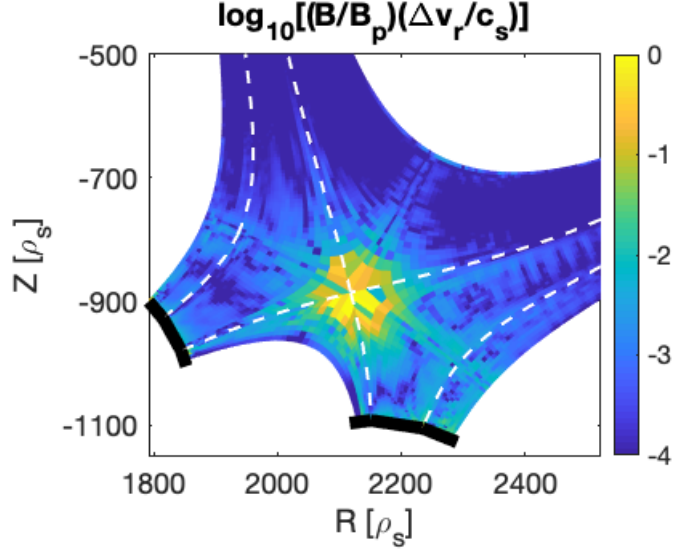
Figure 6: $\log_{10}\left(\dfrac{B}{B_p}\dfrac{\Delta v_r}{c_s}\right)$ evaluated locally for each simulation cell for the WEST simulation.

5.2 Blob radial displacement through a layer with uniform velocity

We can rewrite the approximate condition in Eq. (8) in a more quantitative way: we consider a blob of radial extension $a_{r,X}$ just above the X-point. As the density perturbation front travels along the field line across the radial velocity shear layer, it is displaced radially by the distance $\Delta r = \int_0^{t_l}(v_r - v_0)dt$ where $t_l = l_{||}/c_s = (B/B_p)l_\theta/c_s$ is the time necessary to cross the shear layer of poloidal extension l_θ and v_0 is the radial velocity above the X-point. We consider the blob to be effectively disconnected by the X-point shear layer if $\Delta r \gtrsim a_{r,X}$. As a first approximation, considering the radial velocity uniform across the shear layer, this condition results in

$$\frac{B}{B_p}\frac{\Delta v_r}{c_s} \gtrsim \frac{a_{r,X}}{l_\theta} \tag{9}$$

where $\Delta v_r = v_r - v_0$. We remark that this condition recovers approximately our first estimate in Eq. (8), as the term at the right hand side is typically around 1. Indeed, for our simulation in Fig. 1 the poloidal extension of the shear layer is $l_\theta \sim 53\rho_s$ and the radial blob size at the midplane computed in Ref. [8] with a conditional average technique is $a_r \sim 5\rho_s$, resulting in a radial blob size at the X-point $a_{r,X} = f_x a_r$ with $f_x \leq 14$ in the simulation and the RHS term is therefore $a_{r,X}/l_\theta = 1.32$. Since in this simulation $\Delta v_r \sim 0.02c_s$, Eq. (9) is satisfied for $B_p/B \lesssim 0.015$, similarly to what estimated previously, which is still valid for the X-point velocity shear layer (Fig .5). We remark that the latter provides only an underestimation, since we neglected the effect introduced by the magnetic shear that, as shown in Fig. 3, results in the tilting of the flux tube cross section with respect to the radial direction at the X-point of an angle α, facilitating the filament disconnection by the shear in radial $\mathbf{E} \times \mathbf{B}$. Indeed, the radial projection of the cross section in correspondence of the X-point has then to be multiplied by the tilting factor

$$\Theta = \left[\cos^2\alpha + \sin^2\alpha f_x^4(a_r/a_\theta)^2\right]^{-1/2} \ll 1 \tag{10}$$

since typically $\alpha \sim \pi/4$.

5.3 Blob radial displacement through the poloidal shear layer

We proceed now to the evaluation of the radial displacement Δr resulting from the velocity shear given by the density distribution along the divertor leg described by the model in section 4:

$$\Delta r = \int_0^{t_l} (v_r - v_0)dt = -\frac{T_e}{Bc_s} \int_0^{z_l} \frac{\nabla_z n}{n} \frac{B}{B_p} dz \tag{11}$$

where $t_l = z_l/c_s$ is the time necessary to cross the shear layer of width z_l along the parallel coordinate z and we used $\nabla_\theta = (B/B_p)\nabla_z$. Even though, as it will be discussed further in section 6, the radial velocity above the X-point is usually $v_0 > 0$, here we make the conservative simplifying assumption $v_0 = 0$. We remark that in the surrounding of the magnetic null the poloidal field B_p can be expressed as $B_p = B_p(r,z) \propto re^{az}$ [13], where a is a proportionality constant. The integral in Eq. (11) diverges therefore for the flux surface coinciding with the X-point ($r = 0$), but it can be shown to be finite arbitrarily close to it ($r > 0$). In the following, for simplicity, we give a lower estimate of Δr, by neglecting the z dependency of B_p and substituting in the integral with its value just after the shear layer $B_p(z_l)$, since for z in the interval $[0,\ z_l]$ we have $B_p(z) \leq B_p(z_l)$

$$\Delta r \geq -\frac{T_e}{c_s B_p(z_l)} \int_0^{z_l} \nabla_z \ln \frac{n}{n_X} dz = \frac{T_e}{c_s B_p(z_l)} \mathcal{F} \tag{12}$$

where we define $\mathcal{F} = -\ln\left[n(r,z_l)/n(r,0)\right]$. $\mathcal{F}$ is a function of the shear layer parallel width z_l and of the radial coordinate r, and can be computed directly once the poloidal distribution of the plasma density n is known. Nevertheless, in order to obtain an analytical expression for $\mathcal{F}$, we consider the density distribution across the divertor leg given in Eq. (4,3). $\mathcal{F}$ can then be expressed as a function of the transport parameters D and λ:

$$\mathcal{F} = -\frac{Dz_l}{v_\| \lambda^2} - \ln\frac{1}{2}\text{erfc}\left(\sqrt{\frac{Dz_l}{v_\| \lambda^2}} - r\sqrt{\frac{v_\|}{4Dz_l}}\right) \tag{13}$$

We can further simplify $\mathcal{F}$ by giving an estimate of the shear layer width resulting from our model. This can be done using an analytic approximation of erfc in in Eq. (3), e.g. $\text{erfc}(\chi) \sim 1 - \tanh(\chi\sqrt{\pi}\ln 2)$, and considering the proximity of the divertor leg $r \sim 0$, keeping in mind that $\mathcal{F}$ decreases approximately linearly with r for $r \leq 2\lambda$. The approximated shear layer width along the field line is therefore $z_l \sim \pi(\ln 2)^2 v_\| \lambda^2/D$. By plugging this estimate in Eq. (13), the transport parameters simplify giving $\mathcal{F} = 1.68$.

The condition in Eqs. (8,9), asserting when the poloidal shear of radial velocity can have a role in disconnecting the filaments at the X-point, can then be rewritten as a (weak) function of the transport parameters

$$\frac{B_p}{B} \lesssim \frac{T_e}{B} \frac{\mathcal{F}}{c_s a_{r,X}} \tag{14}$$

where we identified $v_\| \equiv c_s$, and we remind that in general both B_p and $\mathcal{F}$ depend on r, z_l.

The condition in Eq. (14), once again, is always satisfied at the X-point as $B_p = 0$ by definition here, and is further satisfied on a region whose radial extension depends on the plasma and transport parameters and on the details of the magnetic equilibrium. For the WEST simulation using the values resulting form the fitting of the density profiles in the near SOL divertor leg with Eq. (3) i.e. $D = 10^{-3}\rho_s^2\omega_c$, $\lambda = 1.1\rho_s$, with $z_l \sim 2000\rho_s$, $a_r \sim 5\rho_s$ and $a_{r,X} = f_x a_r$ with $f_x \leq 14$ in the simulation, the condition in Eq. (14) results in $B_p/B \lesssim 0.022$, consistently with the value we estimated by applying the approximate condition Eq. (8) directly to the simulation output ($B_p/B \lesssim \Delta v_r/c_s \sim 0.02$). Once again, the latter is an underestimate since we neglected the tilting

9

of the flux tube due to magnetic shear, reducing the radial projection of the filament at the X-point by a factor $\Theta < 1$ (Eq.(10)).

6 Discussion

Summarizing, the disconnection of filaments at the X-point observed in both experiments and turbulence simulations can be due to two mechanisms, namely the deformation of the flux tubes by the high flux expansion and magnetic shear at the X-point, and the poloidal shear of radial $\mathbf{E} \times \mathbf{B}$ velocity, discussed for the first time in this work. Both mechanisms arise naturally in the presence of an X-point, and can act synergistically to decorrelate the density fluctuations in the X-point region resulting in the formation of a quiescent zone, possibly affecting both the blob dynamics at the midplane (i.e. the particle flux to the first wall), and the fluctuating part of the heat loads on the divertor plates. Indeed, a blob of radial and poloidal size at the midplane a_r and a_θ, respectively, at at radial upstream position r and flux expansion in correspondence of the X-point f_x, will be squeezed down to scales where collisional processes dominate and will terminate at the X-point if $a_\theta/\rho_s \lesssim f_x$. Otherwise, blob with bigger poloidal size $a_\theta/\rho_s > f_x$ can survive the X-point squeezing and extend further towards the target plate. These filaments encounter, just below the X-point, the poloidal shear layer of radial $\mathbf{E} \times \mathbf{B}$ velocity. The latter causes the filament to lose coherence if $f_x \lesssim \dfrac{T_e \mathcal{F}}{B_p c_s a_r \Theta}$, where we have rewritten Eq. (14) by recalling $a_{r,X} = f_x a_r \Theta$. The probability of the blob being disconnected by the shear layer decreases with their radial size at the outer midplane a_r and with the poloidal field at the shear layer location (i.e., at fixed f_x, Θ, with the plasma current I_p), and increases with the plasma temperature. This second mechanism can therefore help in suppressing the blobs of bigger poloidal size that would survive the X-point squeezing, resulting in an extended quiescent zone similarly to what has been observed in MAST.

The relative importance of the two disconnection mechanisms could be assessed in a dedicated experiment in which the magnetic configuration (f_x profile, Θ) is kept fixed and i) the plasma temperature is changed scanning the input power, ii) the poloidal field is varied at fixed flux expansion. The quiescent zone could be monitored by fast framing imaging similarly to Ref. [4], and the fluctuation level at the strike point could be measured by Langmuir probes embedded in the divertor. The size of the blob at the midplane, affecting the efficiency of both mechanisms and on which one has close to no control while planning a plasma discharge, needs to be monitored by gas puff imaging or through measurements from reciprocating Langmuir probes.

Furthermore, in section 5.3 we considered the radial velocity above the X-point to be $v_0 = 0$. In general though $v_0 > 0$ due mainly to the naturally outwards motion of blobs the outer midplane, as derived from theoretical models and observed in experiments. As shown in Ref. [8], at the X-point the blob radial velocity is increased such that $v_r/f_x \sim const$ along the field line as the filament tends to keep its alignment with the field line through its motion. This is reflected in the WEST simulation also in the value of the average radial velocity above the X-point $v_0/c_s = 2 \cdot 10^{-3}$. The COMPASS simulation exposed in Ref. [7] exhibits the same feature. Therefore, the value of the shear across the X-point can vary with the direction of the magnetic field. In particular, for favorable drift direction (∇B drift directed towards the X-point), resulting in negative radial $\mathbf{E} \times \mathbf{B}$ below the X-point with $v_0 > 0$, the shear experienced by the blobs would be increased with respect to the reversed field case, where both v_0 and $\mathbf{E} \times \mathbf{B}$ are positive. An experimental evidence of the modification of the fluctuation level at the X-point upon field reversal could therefore be interpreted as the relevance of the poloidal shear in blob disconnection, as the other mechanism (squeezing of flux tubes by flux expansion) would not be influenced by the direction of the magnetic field.

10

If the trends described in this paper are confirmed by the envisaged experiments, whose realization is outside the scope of the present work, one could then think about acting on the magnetic configuration (f_x profile, Θ) or the plasma parameters (I_p, T_e) to enhance or diminish the fluctuation level in the divertor leg, possibly affecting and therefore controlling the fluctuations of the heat loads on the target. We remark that how the disconnection of filaments at the X-point from the target, together with the generation of divertor filaments along the divertor leg [6], affects the final heat loads on the targets is an open question and needs to be investigated extensively both through simulations and experiments in future works.

Furthermore, both mechanisms, always present in the vicinity of the magnetic null, can become even more important in advanced magnetic configurations featuring a secondary X-point along the divertor leg, either in the main SOL (snowflake (SF) divertor, specially in its SF- variant [21]), or at the strike point (X and super-X divertor [22, 23]). The extension of the present analysis to such configurations requires dedicated derivation and numerical modeling and is foreseen for future work.

Finally, we remark that the condition in Eq. (14) is the result of several approximations (e.g. the assumptions $\nabla T_e = 0$, $\nabla v_{||} = 0$ and $v_\perp = 0$) and provides therefore an underestimate of the effectiveness of the poloidal shear of radial velocity in disconnecting the filaments. Dropping the isothermal assumption would result in a steeper plasma potential poloidal gradient (Eq. (6)) as T_e decreases going towards the target, i.e. in a stronger velocity shear Δv_r. The inclusion of the effect of temperature gradients in this model through the coupling with the energy conservation equation and the comparison with anisothermal TOKAM3X simulations are foreseen for future works. The non-uniform parallel velocity along the divertor leg and the perpendicular drifts, helping in redistributing the plasma across the divertor leg below the X-point, which are included in our simulations but not in the analytical model borrowed from Ref. [20], need to be accounted for in this derivation (starting from the continuity Eq. (2)). However, this would need to be done in an iterative way and no simple analytical solution might be possible.

Acknowledgments

References

[1] S.I. Krasheninnikov et al. **Recent theoretical progress in understanding coherent structures in edge and SOL turbulence**. *Journal of Plasma Physics*, **74**:679–717, 2008.

[2] D. Carralero et al. **Experimental validation of a filament transport model in turbulent magnetized plasmas**. *Physical Review Letters*, **115**:215002, 2015.

[3] F. Militello et al. **Scrape off layer profiles interpreted with filament dynamics**. *Nuclear Fusion*, **56**:104004, 2016.

[4] N.R. Walkden et al. **Quiescence near the X-point of MAST measured by high speed visible imaging**. *Nuclear Fusion*, **57**:126028, 2017.

[5] R.J. Maqueda et al. **Intermittent divertor filaments in the National Spherical Torus Experiment and their relation to midplane blobs**. *Nuclear Fusion*, **50**:075002, 2010.

[6] F. Scotti et al. **Divertor leg filaments in NSTX-U**. *Nuclear Fusion*, **58**:126028, 2018.

[7] D. Galassi et al. **Drive of parallel flows by turbulence and largescale E B transverse transport in divertor geometry**. *Nuclear Fusion*, **57**:036029, 2017.

[8] F. Nespoli et al. **3D structure and dynamics of filaments in turbulence simulations of WEST diverted plasmas**. *Nuclear Fusion*, **59**:096006, 2019.

[9] P. Tamain et al. **The TOKAM3X code for edge turbulence fluid simulations oftokamak plasmas in versatile magnetic geometries**. *Journal of Computational Physics*, **321**:606–623, 2016.

[10] F. Scotti et al. **Disconnection of SOL turbulence between the outer midplane and divertor target plate in NSTX**. *Nuclear Fusion*, **accepted for publication**, 2020.

[11] M.V. Umansky et al. **Simulation of turbulence in the divertor region of tokamak edge plasma**. *Journal of Nuclear Materials*, **337 - 339**:266 – 270, 2005.

[12] D.A. Baver and J.R. Myra. **Penetration of filamentary structures into the divertor region of spherical tokamaks**. *Physics of Plasmas*, **22**:110901, 2019.

[13] D. Farina et al. **Effectcs of the magnetic field geometry on the flute-like perturbations near the divertor X point**. *Nuclear Fusion*, **33**:1315, 1993.

[14] D. Galassi et al. **Tokamak Edge Plasma Turbulence Interaction with Magnetic X-point in 3D Global Simulations**. *Fluids*, 4:50, 2019.

[15] S.J. Zweben et al. **Edge and SOL turbulence and blob variations over a large database in NSTX**. *Nuclear Fusion*, **55**:093035, 2015.

[16] N. Fedorczak et al. **Width of turbulent SOL in circular plasmas: A theoretical model validated on experiments in Tore Supra tokamak**. *Nuclear Materials and Energy*, **12**:838–843, 2017.

[17] A. Kirk et al. **L-mode filament characteristics on MAST as a function of plasma current measured using visible imaging**. *Plasma Physics and Controlled Fusion*, **58**:085008, 2016.

[18] C.K. Tsui et al. **Filamentary velocity scaling validation in the TCV tokamak**. *Physics of Plasmas*, **25**:072506, 2018.

[19] J.A. Boedo et al. **Transport by intermittent convection in the boundary of the DIII-D tokamak**. *Physics of Plasmas*, **8**:4826, 2001.

[20] F. Wagner. **A study of the perpendicular particle transport properties in the scrape-off layer of ASDEX**. *Nuclear Fusion*, 5:525, 1985.

[21] D.D. Ryutov and V.A. Soukhanovski. **The snowflake divertor**. *Physics of Plasmas*, **22**:110901, 2015.

[22] M. Kotschenreuther et al. **On heat loading, novel divertors, and fusion reactors**. *Physics of Plasmas*, **14**:072502, 2007.

[23] M. Kotschenreuther et al. **The super X divertor (SXD) and a compact fusion neutron source (CFNS)**. *Nuclear Fusion*, **50**:035003, 2010.